


Article

Fabrication of La₂O₃ Uniformly Doped Mo Nanopowders by Solution Combustion Synthesis Followed by Reduction under Hydrogen

Siyong Gu ^{1,2,*} , Mingli Qin ^{1,*}, Houan Zhang ² and Jidong Ma ²

¹ Institute for Advanced Materials and Technology, University of Science and Technology Beijing, Beijing 100083, China

² Fujian Collaborative innovation center for R&D of coach and special vehicle, Xiamen University of Technology, Xiamen 361024, China; ha_zhang@163.com (H.Z.); jidongustb@126.com (J.M.)

* Correspondence: gu-siyong@163.com (S.G.); qinml@mater.ustb.edu.cn (M.Q.)

Received: 18 October 2018; Accepted: 26 November 2018; Published: 27 November 2018



Abstract: This work reports the preparation of La₂O₃ uniformly doped Mo nanopowders with the particle sizes of 40–70 nm by solution combustion synthesis and subsequent hydrogen reduction (SCSHR). To reach this aim, the foam-like MoO₂ precursors (20–40 nm in size) with different amounts of La₂O₃ were first synthesized by a solution combustion synthesis method. Next, these precursors were used to prepare La₂O₃ doped Mo nanopowders through hydrogen reduction. Thus, the content of La₂O₃ used for doping can be accurately controlled via the SCSHR route to obtain the desired loading degree. The successful doping of La₂O₃ into Mo nanopowders with uniform distribution were proved by X-ray photon spectroscopy and transmission electron microscopy. The preservation of the original morphology and size of the MoO₂ precursor by the La₂O₃ doped Mo nanopowders was attributed to the pseudomorphic transport mechanism occurring at 600 °C. As shown by X-ray diffraction, the formation of Mo₂C impurity, which usually occurs in the direct H₂ reduction process, can be avoided by using the Ar calcination-H₂ reduction process, when residual carbon is removed by the carbothermal reaction during Ar calcination at 500 °C.

Keywords: Mo nanopowder; doping; La₂O₃; solution combustion synthesis; hydrogen reduction

1. Introduction

Molybdenum (Mo) and its alloys have excellent high temperature performance, such as high temperature strength, high creep resistance, low thermal expansion coefficient, and high thermal conductivity [1–3]. Thus, they have been widely used as high-temperature components in the aerospace industry, the nuclear industry, metal processing, and other fields [3–5]. However, the major drawbacks related to the inherent brittleness and high ductile-brittle transition temperature (DBTT) of Mo alloys not only lead to poor toughness at room temperature, but also to inadequate ductility and strength at high temperature, which greatly limits the widespread application of Mo and its alloys. Therefore, decreasing the DBTT to simultaneously improve both ductility and strength of Mo alloy at room temperature has become a well-known major goal over recent decades [5,6]. As previously reported [2,7–9], the addition of rare-earth oxides, such as La₂O₃, Y₂O₃, and Gd₂O₃ into Mo alloys via various doping routes to form rare-earth oxide doped Mo alloys can obviously decrease DBTT. Thus, the rare-earth oxide doped Mo alloys have high toughness and strength at both room and high temperatures. Moreover, the preparation of nano-sized oxide particles with uniform dispersion into the Mo grain and the engineering of Mo grains at nanoscale are key factors for obtaining high performance Mo alloys. Recently, it was clearly demonstrated that Mo alloys can be achieved using

high quality La_2O_3 doped Mo powder synthesized via the liquid–liquid doping route (L-L doping) [2]. Therefore, the rare-earth oxide doped powders composed of nanoparticles with a highly dispersed oxide phase are a crucial factor to obtain high-performance Mo alloys. So far, the conventional doping routes, i.e., solid Mo powders mixed with solid oxide particles (S-S doping) [7,10], solid Mo powders mixed with liquid oxide particles (S-L doping) [11–13], and liquid Mo-based compounds mixed with liquid oxide particles (L-L doping) [2,14], have been applied to prepare the designed rare-earth doped Mo powders. Among these strategies, the L-L doping route is the most attractive because it allows mixing of the precursors at the molecular level.

As previously reported [15], the performance of La_2O_3 doped Mo alloys exceeds those of other doped by rare-earth oxides (i.e., Nd_2O_3 , Sm_2O_3 , Gd_2O_3 , and Y_2O_3). In addition, previous studies about the doping content of La_2O_3 indicated that the doping content of La_2O_3 exceeds 2.0 wt.%, which cannot improve the properties of molybdenum alloys [2,16]. Cheng et al. [8] studied the properties of Mo alloy with different doping contents of La_2O_3 , and the results showed that the Mo alloy with 0.5–1.0 wt.% La_2O_3 doping simultaneously achieve high strength and great elongation.

Solution combustion synthesis (SCS) is a versatile, energy-efficient, and mass production suitable method that has been used to fabricate several types of nano-sized oxides with different physical and chemical properties [17–19]. In addition, SCS is also one of the proper methods to prepare uniformly doped nano-sized oxides, such as Al-doped ZnO nanoparticles [20], Sn-doped $\alpha\text{-Fe}_2\text{O}_3$ nanoparticles [21], and $\text{Fe}^{3+}\text{-W}_{18}\text{O}_{49}$ nanoparticles [22], because precursor mixing at the molecular level ensured that the doped element can be distributed homogeneously throughout the matrix.

In our previous work [23], foam-like MoO_2 nanoparticles, assembled by 20–30 nm nanoparticles, were successfully fabricated by SCS. In this paper, a facile method based on the SCS and subsequent hydrogen reduction route (SCSHR) is proposed to prepare La_2O_3 uniformly doped Mo nanopowders with various La_2O_3 loading degrees ranging from 0 to 1.2 wt.%. In fact, the SCSHR route not only ensures the high dispersion of La_2O_3 as a result of mixing at the molecular level, but also the formation of nanopowders with homogeneous distribution of the oxide nanoparticles. The crystalline phase evolution, morphology, elemental composition, and reduction processes have been studied in detail. Moreover, the formation mechanism of La_2O_3 doped Mo nanopowders has been discussed.

2. Experimental

2.1. Materials

Hexaammonium molybdate ($(\text{NH}_4)_6\text{Mo}_7\text{O}_{24}\cdot 4\text{H}_2\text{O}$, AHM, Sinopharm Chemical Reagent Co., Ltd., Shanghai, China), lanthanum(III) nitrate hexahydrate ($\text{La}(\text{NO}_3)_3\cdot 6\text{H}_2\text{O}$, Sinopharm Chemical Reagent Co., Ltd.), ammonium nitrate ($(\text{NH}_4)\text{NO}_3$, Sinopharm Chemical Reagent Co., Ltd.), and glycine ($\text{C}_2\text{H}_5\text{NO}_2$, Sinopharm Chemical Reagent Co., Ltd.) were of analytical grade and used as received without any further purification.

2.2. Synthesis of La_2O_3 Doped MoO_2 Precursor

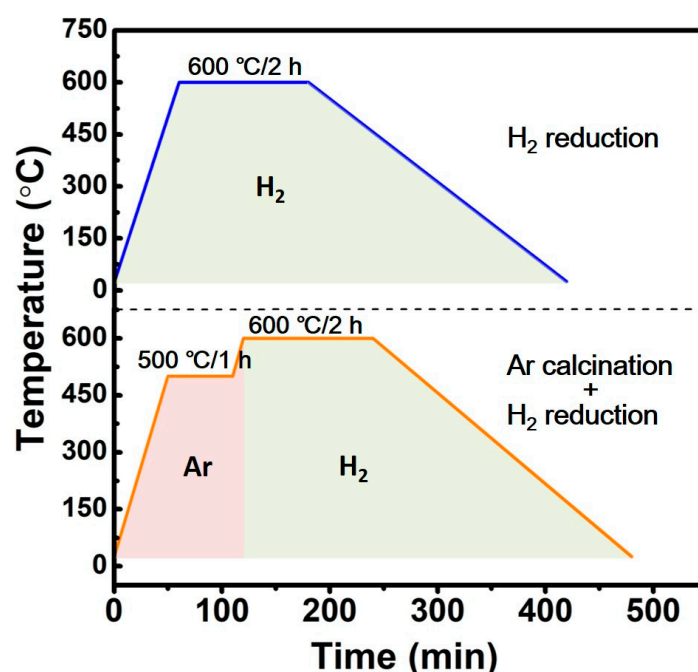
MoO_2 precursor with different La_2O_3 contents were synthesized via SCS using a mixture of AHM, $\text{La}(\text{NO}_3)_3\cdot 6\text{H}_2\text{O}$, $(\text{NH}_4)\text{NO}_3$, and glycine as raw materials, as shown in Table 1, with different La_2O_3 content (0, 0.3, 0.6, 0.9, and 1.2 wt.%, i.e., the mass ratio of La_2O_3 and Mo), and labeled as P-LM0, P-LM3, P-LM6, P-LM9, and P-LM12, respectively. First, the mixture of metallic salts was dissolved in 100 mL of deionized water under magnetic stirring until a homogeneous solution was obtained. The solution was then poured into a 1000 mL beaker and heated at 160 °C in air using a temperature-controlled electric heating furnace. After heating for about 5 min at 160 °C, as soon as the solvent had evaporated, and a gelatinous mass was formed, an instantaneous combustion reaction occurred, accompanied by expansion of the gelatinous mass and the evolution of gas. The whole combustion reaction process lasted for less than 1 min and a foamy and black MoO_2 precursor doped with different La_2O_3 contents, i.e., P-LM0, P-LM3, P-LM6, P-LM9, and P-LM12, was synthesized.

Table 1. Amount of raw materials used for the solution combustion synthesis (SCS) of La₂O₃ doped MoO₂ precursors.

Precursor	La ₂ O ₃ Doping Content (wt.%)	AHM (mol)	NH ₄ NO ₃ (mol)	C ₂ H ₅ O ₂ N (mol)	La(NO ₃) ₃ (mol)
P-LM0	0	0.01	0.2	0.10	0
P-LM3	0.3	0.01	0.2	0.10	0.00012
P-LM6	0.6	0.01	0.2	0.10	0.00025
P-LM9	0.9	0.01	0.2	0.10	0.00037
P-LM12	1.2	0.01	0.2	0.10	0.00050

2.3. Hydrogen Reduction of Mo-Based Precursor

Lanthanum-based MoO₂ precursors (P-LM0, P-LM3, P-LM6, P-LM9, and P-LM12) were reduced by using two different reduction processes, i.e., a direct H₂ reduction process and an Ar calcination-H₂ reduction process. The detailed reduction procedure is shown in Figure 1, and the reduced products are marked as LM0, LM3, LM6, LM9, and LM12, respectively.

**Figure 1.** Direct H₂ reduction process and Ar calcination-H₂ reduction process for MoO₂ precursors.

2.4. Characterization

The crystalline phases of the samples were analyzed using an X-ray diffractometer (Rigaku, D/max-RB12, Tokyo, Japan) with Cu K α radiation, and a 2 θ angle from 10° to 90° with 0.02° increments. The chemical composition at the surface was established using X-ray photoelectron spectroscopy (XPS, Fison VG ESCA210, West Sussex, England). The morphology and size distribution of the nanoparticles were investigated by field emission scanning electron microscopy (FE-SEM, Zeiss, ULTRA 55, Jena, Germany). Transmission electron microscopy (TEM) and high-resolution transmission electron microscopy (HRTEM) were performed on a transmission electron microscope (FEI, Tecnai G2 F20, Hillsboro, OR, USA) with an acceleration voltage of 200 kV. The carbon content in precursors and reduced samples was measured with a carbon/sulfur analyzer (NCS CS-2800, Beijing, China), and their La content was determined by inductively coupled plasma optical emission spectrometry (ICP-OES, Agilent 720, Santa Clara, CA, USA). The La₂O₃ content of the reduced samples was calculated based on the result of the La content.

3. Results and Discussion

3.1. Phases and Morphology of Precursor

A schematic diagram of the preparation of La_2O_3 uniformly doped Mo nanopowders via the SCSHR route is shown in Figure 2. First, MoO_2 precursors with different La_2O_3 contents were synthesized via SCS using AHM, lanthanum nitrate, ammonium nitrate, and glycine as a molybdenum source, La source, oxidizer, and fuel, respectively. All raw materials were mixed and then heated at $160\text{ }^\circ\text{C}$ in air. After about 5 min, an instantaneous combustion reaction occurred, which was accompanied by the evolution of a large amount of gas. The combustion process took less than 1 min and the target precursor samples were synthesized. Next, the obtained precursors were used to prepare La_2O_3 doped Mo nanopowders by a direct H_2 reduction process and an Ar calcination- H_2 reduction process, respectively. The detailed reduction procedure is shown in Figure 1.

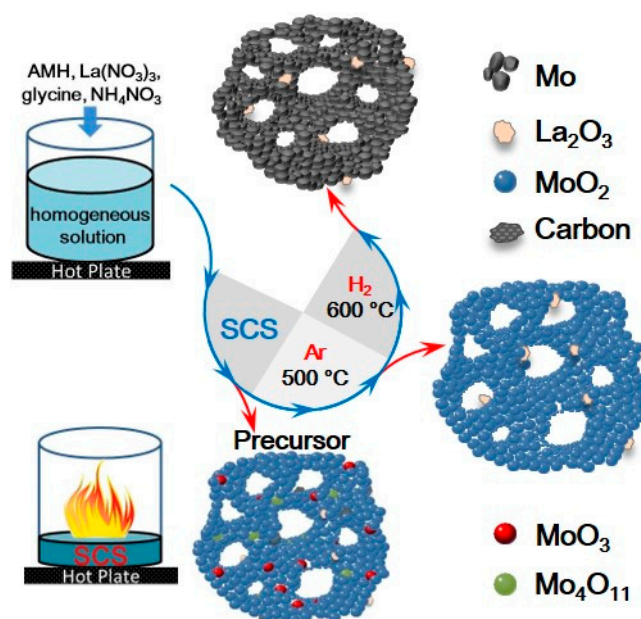


Figure 2. Schematic diagram describing the preparation of La_2O_3 uniformly doped Mo nanopowders via the SCSHR route.

Figure 3 shows the XRD patterns of the different La_2O_3 doped precursors, synthesized by SCS. For all precursors, the diffractograms display the main diffraction peaks, which are indexed as monoclinic MoO_2 (ICDD No. 78-1069). However, extremely small diffraction peaks corresponding to MoO_3 and Mo_4O_{11} phases are also observed in all XRD patterns, indicating that part of the MoO_2 on the surface underwent oxidation in air. It was noted that both diffraction peaks of 2θ of 26 and 29.5 two-theta degree appeared in the P-LM9 precursor sample, indicating that P-LM9 may contain more MoO_3 phases than other samples. In addition, lanthanide compounds, such as La_2O_3 and $\text{La}(\text{OH})_3$ diffraction peaks were not observed for P-LM3, P-LM6, P-LM9, and P-LM12 samples, which was due to the low content of the La element. Nano-sized La_2O_3 has been synthesized by SCS in earlier studies [24–26]. Gangwar et al. [24] reported that a pure La_2O_3 phase can be synthesized by SCS followed by calcination treatment, while La_2O_3 converts to $\text{La}(\text{OH})_3$ upon exposure to the atmosphere due to its hygroscopic nature.

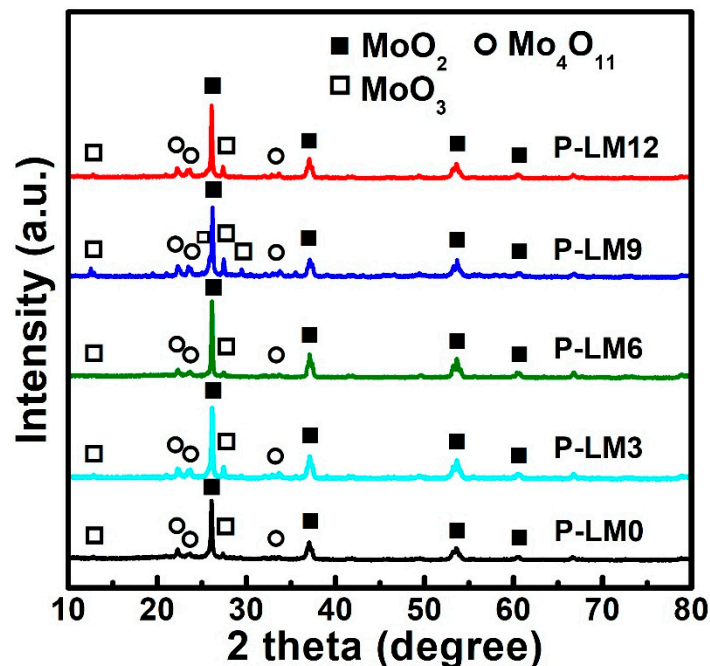


Figure 3. XRD patterns of MoO₂ precursors doped with different La₂O₃ content and synthesized by SCS.

The morphology and microstructure of the precursors were assessed by FE-SEM. Representative images are shown in Figure 4. It can be observed that the P-LM0 precursor sample has a foam-like morphology, as shown in Figure 4a, which is the unique typical morphology obtained by the SCS method. Figure 4b shows that the foam-like P-LM0 is composed of MoO₂ nanoparticles with sizes of 20–40 nm as a result of particle agglomeration due to the high surface energy of MoO₂ nanoparticles. Similarly, the morphology of La₂O₃ doped precursors, i.e., P-LM3, P-LM6, P-LM9, and P-LM12, still maintain the foam-like morphology and particle agglomeration. In addition, the particle size of La₂O₃ doped precursors does not change significantly, indicating that the morphology and particle size of precursors is not affected when doping with low La₂O₃ amounts, as shown in Figure 4c–f. However, due to the low loading degree of La₂O₃, the La₂O₃ nanoparticles are difficult to see in these images.

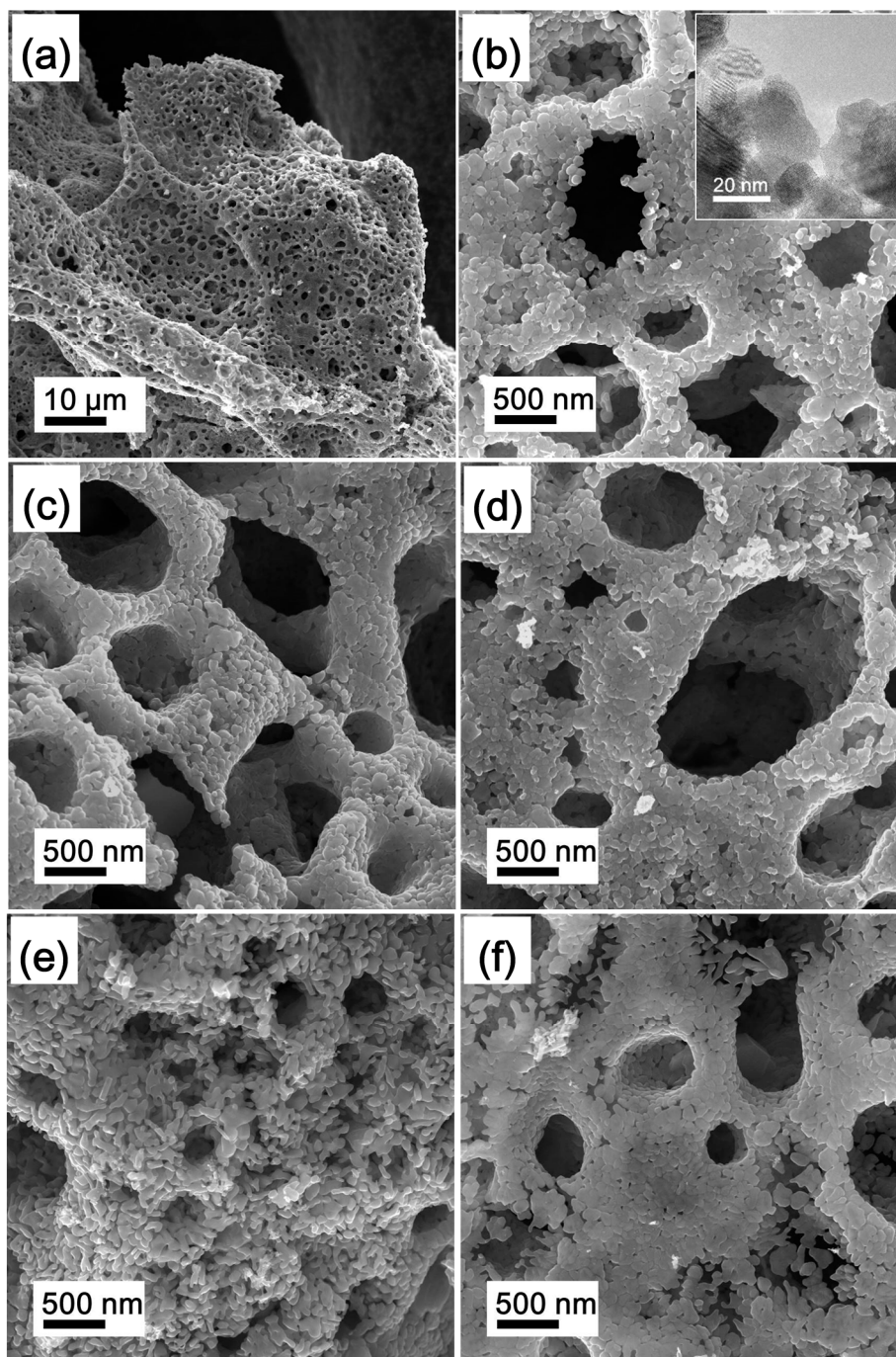


Figure 4. FE-SEM images of MoO₂ precursors for (a,b) P-LM0, (c) P-LM3, (d) P-LM6, (e) P-LM9, and (f) P-LM12; the inset of (b) shows the corresponding TEM image.

To clarify whether La₂O₃ has been successfully doped into the precursor, XPS was performed. Figure 5 shows a survey scan, La 3d spectra, and Mo 3d high-resolution spectra for each precursor. As shown in Figure 5a, no peak of La 3d was observed in P-LM0. However, after La₂O₃ doping, peaks corresponding to La 3d_{3/2} and La 3d_{5/2} appeared whose intensities increase as the amount of La₂O₃ increases in the sample, clearly showing the successful doping of La₂O₃ into MoO₂ precursors. The Mo 3d high-resolution spectra for each precursor display five peaks at 232.8 eV (Mo⁴⁺3d_{3/2} in MoO₂), 299.6 eV (Mo⁴⁺3d_{5/2} in MoO₂), 231.3 eV (Mo⁶⁺3d_{5/2} in MoO₃), 235.9 eV (Mo⁶⁺3d_{3/2} in MoO₃), and 234.4 eV (Mo⁵⁺3d_{3/2} in Mo₄O₁₁), as shown in Figure 5b–f. On the basis of these peaks, the contents of MoO₂, MoO₃, and Mo₄O₁₁ were calculated, and the results are listed in Table 2. As shown,

the contents of impurities, such as MoO_3 and Mo_4O_{11} , were found to be quite high, which far exceeds that indicated by the Rietveld refinement XRD result of a previous study by our research group [27]. This result can be related to the XPS technique, which can analyze only the surface with an information depth of up to 10 nm and can be affected by surface oxidation of the MoO_2 nanoparticles.

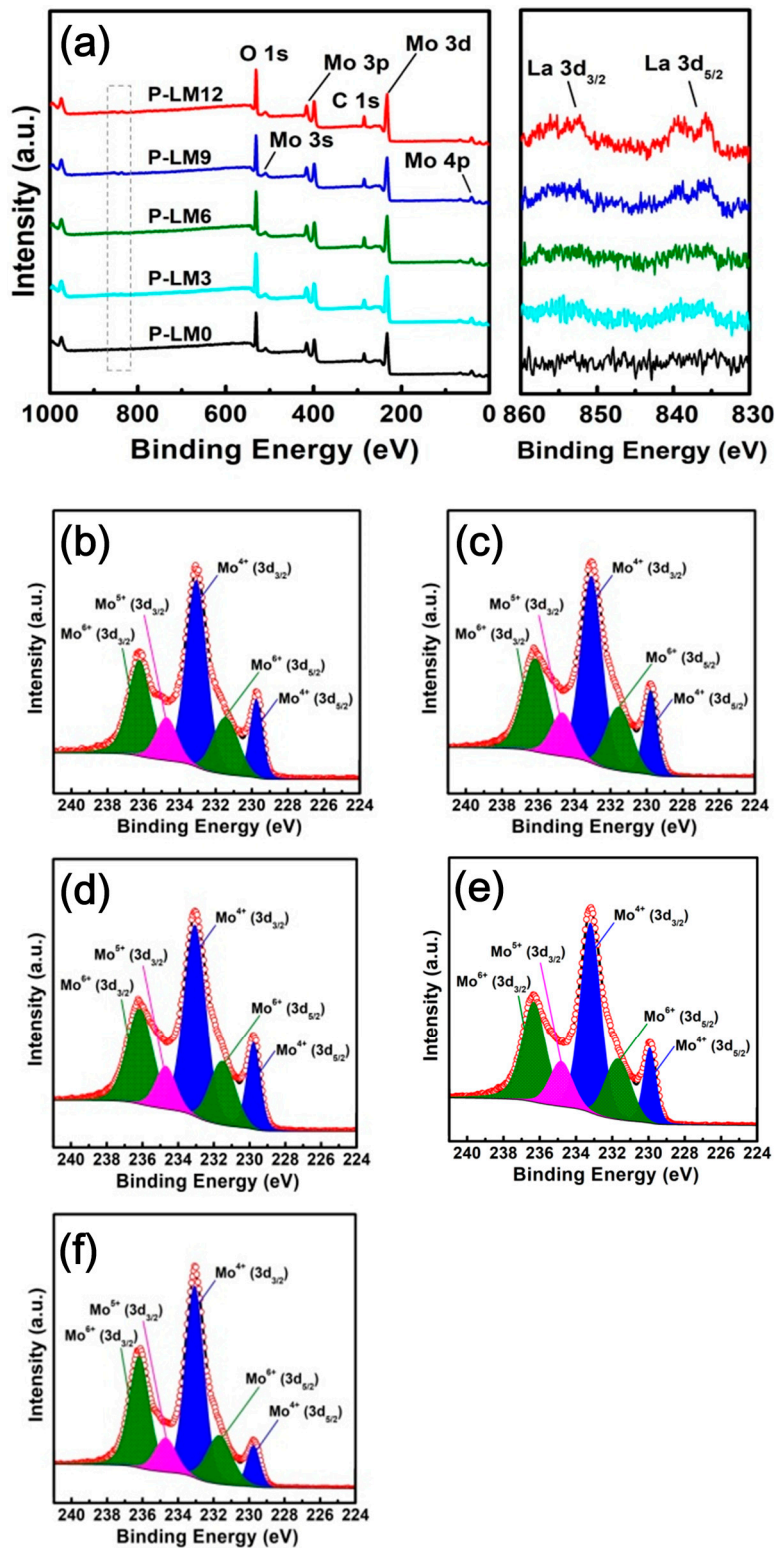


Figure 5. (a) XPS survey scan and La 3d spectra of each MoO_2 precursor. Mo 3d high-resolution spectra of (b) P-LM0, (c) P-LM3, (d) P-LM6, (e) P-LM9, and (f) P-LM12.

Table 2. Contents of MoO₂, MoO₃, and Mo₄O₁₁ in each MoO₂ precursor calculated based on the XPS peak area for Mo 3d.

Precursor	MoO ₂ (wt.%)	MoO ₃ (wt.%)	Mo ₄ O ₁₁ (wt.%)
P-LM0	52.6	38.8	8.6
P-LM3	51.7	38.7	9.6
P-LM6	51.0	39.1	9.9
P-LM9	48.9	41.6	9.3
P-LM12	48.6	42.8	8.6

Table 3 shows the content of C and La elements in each precursor. As observed, each precursor contains traces of carbon. The La content is close to the theoretical content, indicating that the La element is not lost through the SCS method, which ensures the accuracy of La doping.

Table 3. Content of C and La element in each MoO₂ precursor.

Precursors	P-LM0	P-LM3	P-LM6	P-LM9	P-LM12
Elements C (wt.%)	0.27	0.17	0.20	0.18	0.13
Elements La (wt.%)	0	0.13	0.38	0.59	0.81

3.2. Preparation of La₂O₃ Doped Mo Nanopowders

As shown in Figure 1, the P-LM0, P-LM3, P-LM6, P-LM9, and P-LM precursors were reduced by both direct H₂ reduction and Ar calcination-H₂ reduction processes. The corresponding reduction products are referred to as LM0, LM3, LM6, LM9, and LM12 hereafter.

The XRD patterns of the products reduced by direct H₂ reduction and Ar calcination-H₂ reduction process are illustrated in Figures 6 and 7, respectively. As shown in Figure 6, the main diffraction peaks displayed by all diffractograms correspond to the Mo phase while no evidence for MoO₂ peaks is found. This suggests that MoO₂ and impurities (MoO₃ and Mo₄O₁₁) were completely reduced to the metallic Mo phase. Yet, a small diffraction peak at around 38° can be observed in each diffraction pattern. It is attributed to the Mo₂C phase, which may result from the reaction between residual carbon and MoO₂ (or MoO₃, Mo₄O₁₁). On the other hand, the XRD patterns of products obtained by the Ar calcination-H₂ reduction process, as shown in Figure 7, shows that zero-valent Mo is the only crystalline phase while Mo₂C does not appear anymore, clearly suggesting that the formation of Mo₂C can be avoided via rational preparation of La₂O₃ doped Mo powders by the Ar calcination-H₂ reduction process. Indeed, the C content was extremely low, i.e., 0.046, 0.043, 0.053, 0.051, and 0.042 wt.% for LM0, LM3, LM6, LM9, and LM12, respectively, as listed in Table 4. Moreover, the C content was much lower than that of samples obtained by direct H₂ reduction. Therefore, in light of these results, it can be stated that the impurity-free La₂O₃ doped Mo powders can be successfully synthesized by the Ar calcination-H₂ reduction process.

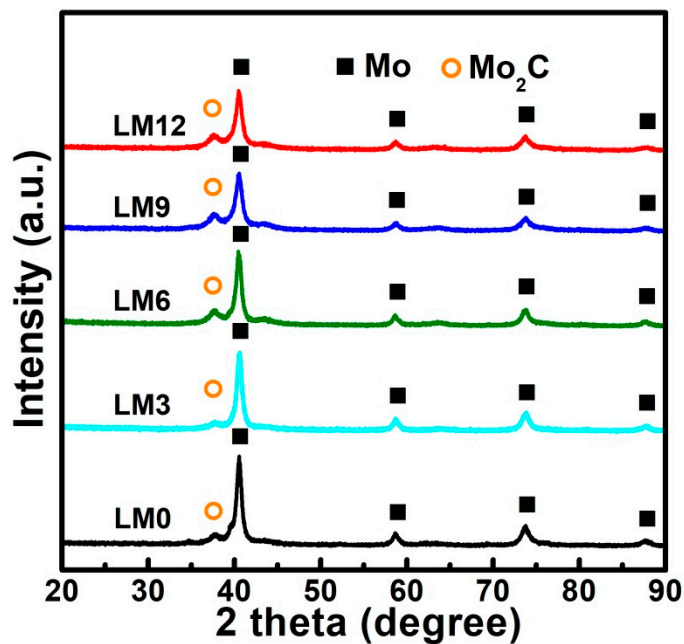


Figure 6. XRD patterns of products reduced by the direct H₂ reduction process.

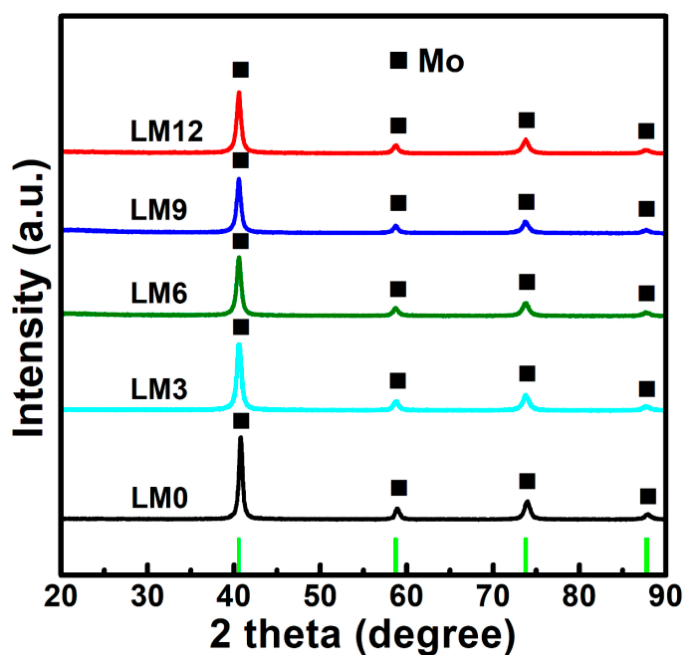


Figure 7. XRD patterns of products reduced by the Ar calcination-H₂ reduction process.

Table 4. The content of C in the products reduced through different reduction processes.

Content	Process	Samples				
		LM0	LM3	LM6	LM9	LM12
C (wt.%)	H ₂ /600 °C	0.286	0.219	0.241	0.236	0.183
	Ar/500 °C + H ₂ /600 °C	0.046	0.043	0.053	0.051	0.042

However, as mentioned above, the low amount of La₂O₃ did not allow its detection by XRD in any of the samples. Regarding Mo, the full width at half maxima (FWHM) of the peak was appropriate to calculate the crystallite size of Mo obtained by the Ar calcination-H₂ reduction process by applying

the Scherrer equation. Hence, crystallites of 28.7, 24.3, 23.8, 22.7, and 21.9 nm were obtained for LM0, LM3, LM6, LM9, and LM12, respectively.

Figure 8 shows the XPS survey scan and La 3d spectra of La₂O₃ doped Mo nanopowders obtained by the Ar calcination-H₂ reduction process and Mo 3d high-resolution spectra for the P-LM9 and LM9 sample. As shown in Figure 8a, the increase in La₂O₃ doping resulted in more intense La 3d peaks, underlying the doping of Mo powders with La₂O₃. Figure 8b comparatively displays the Mo 3d high-resolution spectra of P-LM9 and LM9. It can be noticed that a new peak at 280.2 eV appeared in Mo 3d high-resolution spectra of LM9, which is ascribed to metallic Mo. Thus, this is evidence of the formation of a metallic Mo phase in the sample. In addition, well-shaped peaks corresponding to MoO₂, MoO₃, and Mo₄O₁₁ phases are observed for LM9, suggesting that Mo nanoparticles at the surface were oxidized in air. The Mo 3d high-resolution spectra for the other samples, i.e., LM0, LM3, LM6, and LM12, show similar characteristics to that of LM9.

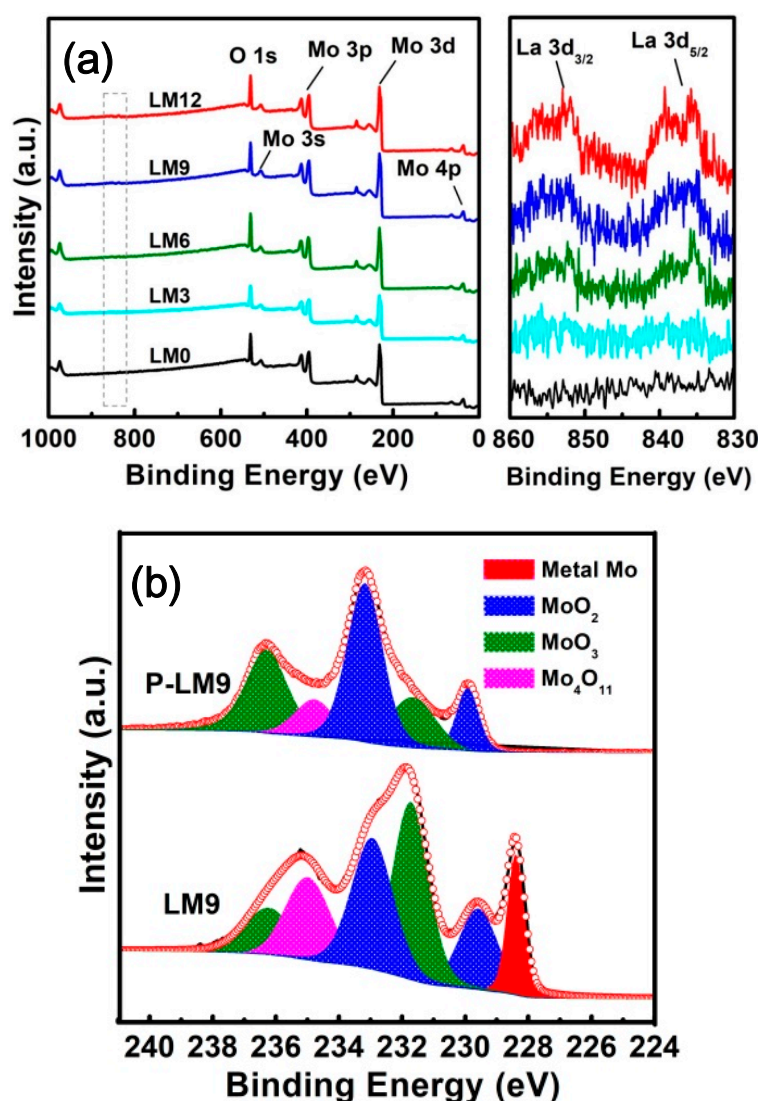


Figure 8. (a) XPS survey scan and La 3d spectra of La₂O₃ doped Mo nanopowders obtained by the Ar calcination-H₂ reduction process, and (b) Mo 3d high-resolution spectra of P-LM9 and LM9.

ICP-OES was used to analyze the La content in La₂O₃ doped Mo nanopowders reduced by the Ar calcination-H₂ reduction process. Accordingly, the La₂O₃ contents as calculated from La content of LM3, LM6, LM9, and LM12 samples are 0.27, 0.64, 0.88, and 1.16 wt.%, respectively. These values

are close to the theoretical values, showing that the synthetic approach used herein to prepare La_2O_3 doped Mo powders is suitable for a complete incorporation of the doping element.

FE-SEM images of La_2O_3 doped Mo nanopowders reduced by the Ar calcination- H_2 reduction process are displayed in Figure 9. Aggregates composed of nanoparticles are clearly seen for each product. The foam-like morphology seen in Figure 9d indicates that the samples maintain the original morphology of MoO_2 precursor during the reduction process. The average particle sizes, obtained from the SEM images, increase as the amount of La_2O_3 decreases ($43\text{ nm (LM12)} > 49\text{ nm (LM9)} > 58\text{ nm (LM6)} > 63\text{ nm (LM3)} > 68\text{ nm (LM0)}$), revealing the inhibition of the segregation process induced by La_2O_3 doping.

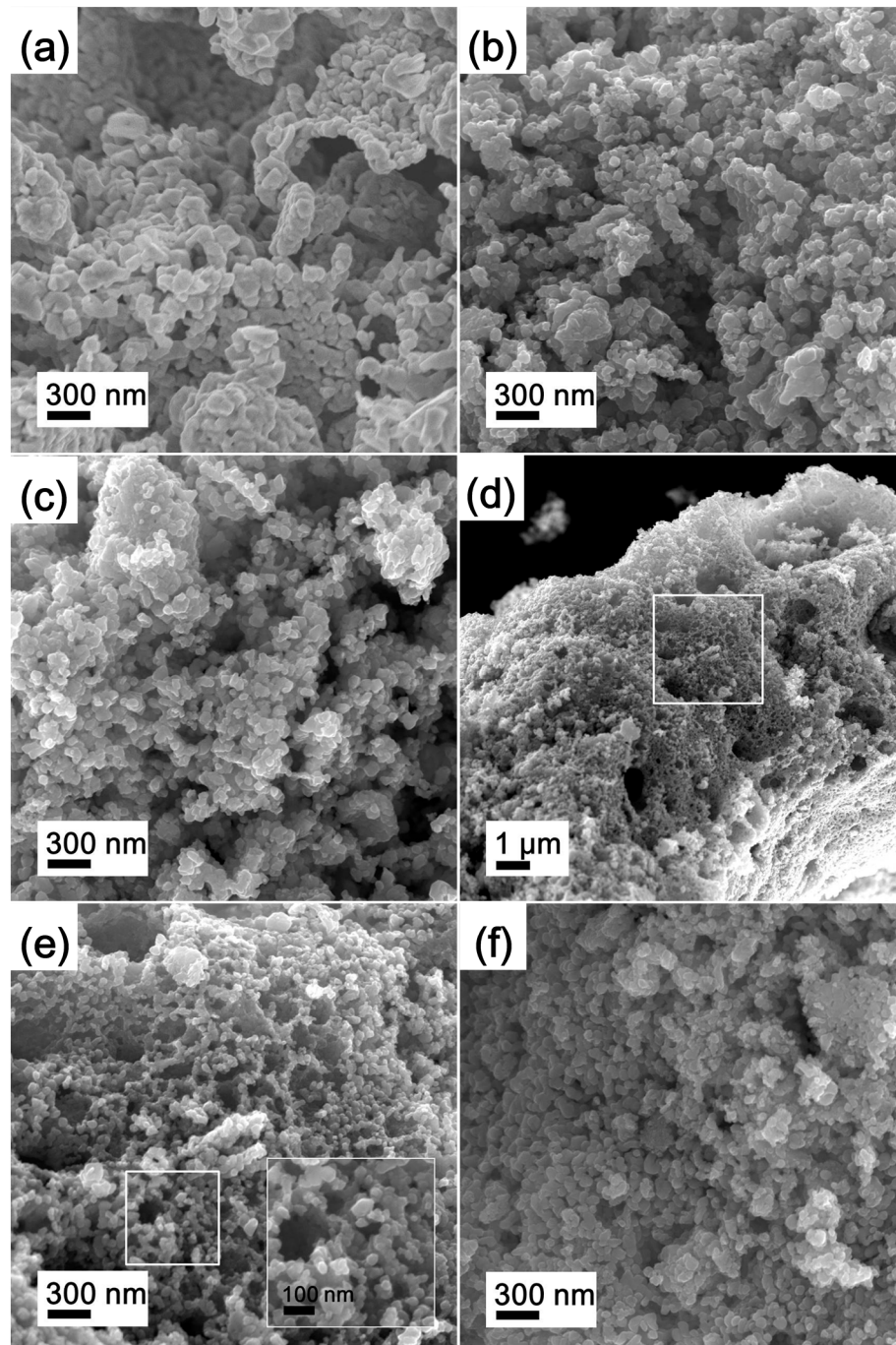


Figure 9. FE-SEM images of La_2O_3 doped Mo nanopowders for (a) LM0, (b) LM3, (c) LM6, (d,e) LM9, and (f) LM12 reduced by the Ar calcination- H_2 reduction process.

TEM micrographs of the LM9 product reduced by the Ar calcination-H₂ reduction process are shown in Figure 10. Figure 10a displays aggregates of irregular shapes of Mo nanoparticles. The corresponding selected-area diffraction electron patterns (SAED), shown in the inset, exhibit a polycrystalline ring pattern, indicating that the aggregate consists of Mo nanoparticles, which agrees with the FE-SEM observations. The elemental mapping images, shown in Figure 10b, demonstrate the uniform distribution of Mo, La, and O elements throughout the particles, and confirm the uniform La₂O₃ doping into Mo nanopowders via the SCSHR route. It is worth mentioning that the relatively high content of O observed in the O element mapping image may be explained by (i) its origin in La₂O₃ and (ii) the oxidation of surface Mo nanoparticles.

Figure 10c,d shows the HRTEM images taken from the selected area in Figure 10a. Two different lattice fringes are clearly observed. Rich lattice fringes with spacing of 0.22 nm correspond to the (110) plane of metallic Mo. Other small lattice fringes are clearly seen at the edge of particles while lattice spacing of 0.32 nm, which agrees well with the (222) crystalline plane of La₂O₃. This result further confirms the successful doping of La₂O₃ into Mo nanopowders.

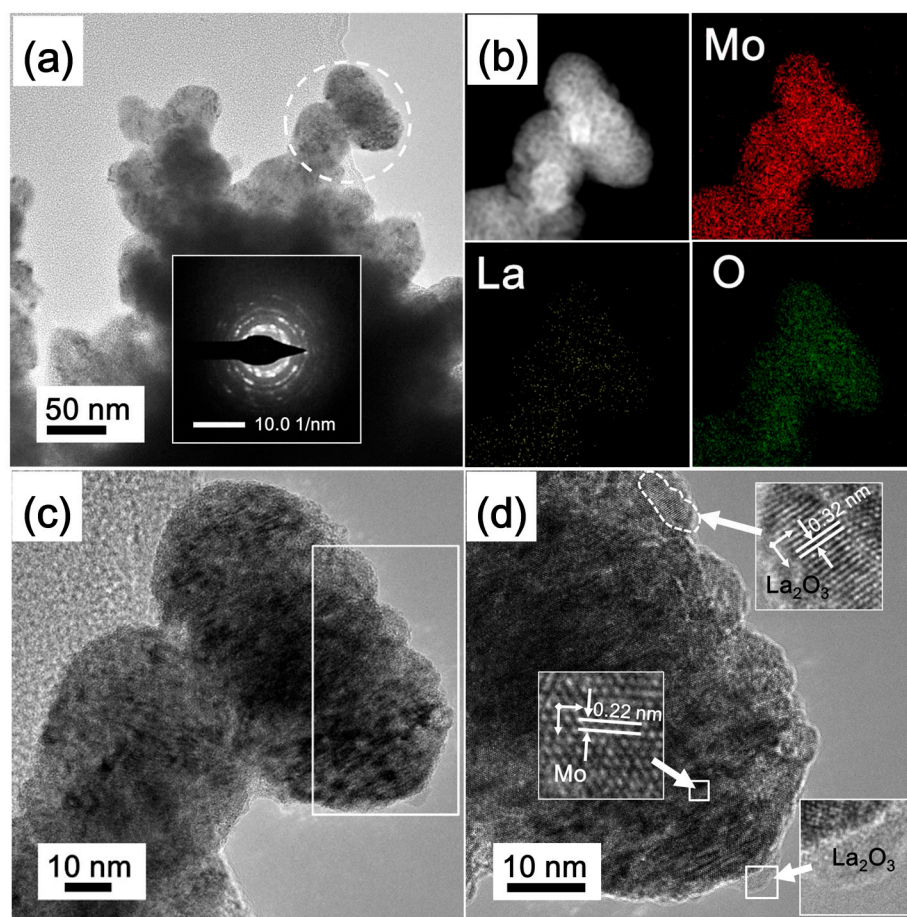
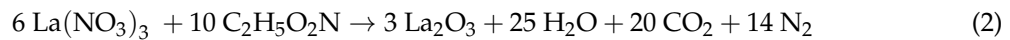
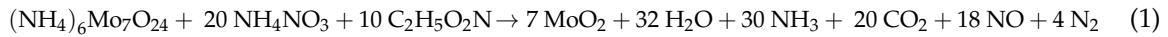


Figure 10. (a) TEM, (b) elemental mapping, (c,d) HRTEM images of La₂O₃ doped Mo nanopowders (LM9 sample); the inset of (a) shows the corresponding SAED pattern; the insets of (d) show the lattice fringes of metallic Mo and La₂O₃.

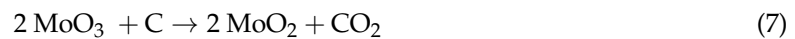
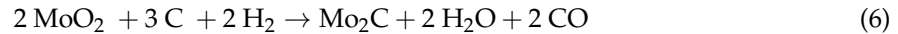
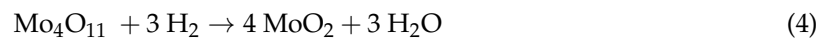
3.3. Formation Mechanism of La₂O₃ Doped Mo Nanopowders

According to theory, SCS involves strong oxidation–reduction reactions. In this reaction system, the La₂O₃ doped MoO₂ precursors were formed by Equation (1) and Equation (2). Furthermore, a large amount of gases generated led to the formation of foam-like morphology [23]. Because the SCS method involves reactions of precursors in solution, the incorporation of the entire amount of doping element is ensured, as well as the uniform distribution of La₂O₃ into the host material.



Recent studies have shown that the reduction mechanism of MoO₂ to Mo under H₂ depends on the experimental conditions, in particular, the temperature of reduction [28]. The reduction reaction obeys the chemical vapor transport (CVT) mechanism, when the reaction temperature is above 923 K (650 °C). When the reaction temperature is lower than 883 K (610 °C), the mechanism is a pseudomorphic transport mechanism, which results in the nucleation and growth of Mo inside MoO₂ particles. Thus, the Mo products will retain the morphology and size of the initial MoO₂ particles. In light of these results, the preservation of the foam-like morphology and nanostructure of the MoO₂ precursor by the La₂O₃ doped Mo products obtained at 600 °C is explained.

When the precursors were prepared by the direct H₂ reduction process, the impurities consisting of MoO₃ and Mo₄O₁₁ were reduced to MoO₂ based on Equations (3) and (4) [29], respectively. At 600 °C, Equation (5) takes place, forming metallic Mo nanoparticles. Furthermore, an insignificant amount of Mo₂C impurity formed as a result of the carbothermal reduction in hydrogen of MoO₂ [27,30,31], as shown by Equation (6). La₂O₃ does not undergo any phase transition due to its high thermodynamic stability.



When the precursors were calcined in Ar at 500 °C, residual carbon was completely consumed via carbothermal reduction, i.e., Equations (7) and (8). Therefore, the La₂O₃ doped Mo nanopowders without Mo₂C impurity were formed via the Ar calcination-H₂ reduction process.

4. Conclusions

Mo nanopowders doped with different amounts of La₂O₃, i.e., 0, 0.27, 0.64, 0.88, and 1.16 wt.%, were prepared via the SCSHR route, which allowed a homogeneous distribution of the dopant while preserving the theoretical loading degree. The MoO₂ precursors with different content of La₂O₃, synthesized by SCS, displayed similar foam-like morphology and particle sizes of 20–40 nm. Then, La₂O₃ uniformly doped Mo nanopowders were prepared via different reduction processes, i.e., the direct H₂ reduction and Ar calcination-H₂ reduction. Compared to the direct H₂ reduction processes, the Ar calcination-H₂ reduction process led to La₂O₃ uniformly doped Mo nanopowders without Mo₂C impurities. La₂O₃ uniformly doped Mo nanopowders were composed of nanoparticles with sizes of 40–70 nm, which was in line with the decrease in La₂O₃. Hence, La₂O₃ doped Mo nanopowders retained the original morphology and size of the MoO₂ precursor because the formation of Mo nanoparticles reduced at 600 °C obeys the pseudomorphic transport mechanism. The formation of Mo₂C impurity was noticed due to the carbothermal reduction occurring when samples were directly reduced under H₂. On the other hand, when the Ar calcination-H₂ reduction process was applied to form lanthana-based materials, the residual carbon was completely consumed via the carbothermal reduction during the calcination in Ar at 500 °C and thus La₂O₃ doped Mo nanopowders without Mo₂C impurity can be successfully prepared. The results obtained herein are valuable to

recommend the SCSHR method for preparation of other oxide doped refractory metal nanopowders (e.g., tungsten and niobium).

Author Contributions: Investigation, S.G.; Methodology, S.G. and M.Q.; Resources, M.Q., H.Z. and J.M.; Writing—original draft preparation, S.G.; Writing—review and editing, M.Q., H.Z. Finding acquisition, M.Q., H.Z. and J.M.

Funding: This research was funded by the Programs of the National Natural Science Foundation of China (Grant No. 51574031), the National Key R&D Program of China (Grant No. 2017YFB0305600), the Educational Scientific Research Project of Young Teachers in Fujian Province (Grant No. JAT170402), and the Program for Innovative Research Team in Science and Technology in Fujian Province University (IRTSTFJ).

Conflicts of Interest: The authors declare no conflict of interest.

References

1. Perepezko, J.H. The hotter the engine, the better. *Science* **2009**, *326*, 1068–1069. [[CrossRef](#)] [[PubMed](#)]
2. Liu, G.; Zhang, G.J.; Jiang, F.; Ding, X.D.; Sun, Y.J.; Sun, J.; Ma, E. Nanostructured high-strength molybdenum alloys with unprecedented tensile ductility. *Nat. Mater.* **2013**, *12*, 344–350. [[CrossRef](#)] [[PubMed](#)]
3. Lenchuk, O.; Rohrer, J.; Albe, K. Atomistic modelling of zirconium and silicon segregation at twist and tilt grain boundaries in molybdenum. *J. Mater. Sci.* **2016**, *51*, 1873–1881. [[CrossRef](#)]
4. Zhou, Y.; Gao, Y.; Wei, S.; Pan, K.; Hu, Y. Preparation and characterization of Mo/Al₂O₃ composites. *Int. J. Refract. Met. Hard Mater.* **2016**, *54*, 186–195. [[CrossRef](#)]
5. El-Genk, M.S.; Tournier, J.M. A review of refractory metal alloys and mechanically alloyed-oxide dispersion strengthened steels for space nuclear power systems. *J. Nucl. Mater.* **2005**, *340*, 93–112. [[CrossRef](#)]
6. Conduit, B.D.; Jones, N.G.; Stone, H.J.; Conduit, G.J. Probabilistic design of a molybdenum-base alloy using a neural network. *Scr. Mater.* **2018**, *146*, 82–86. [[CrossRef](#)]
7. Wang, K.S.; Tan, J.F.; Hu, P.; Yu, Z.T.; Yang, F.; Hu, B.L.; Song, R.; He, H.C.; Volinsky, A.A. La₂O₃ effects on TZM alloy recovery, recrystallization and mechanical properties. *Mater. Sci. Eng. A* **2015**, *636*, 415–420. [[CrossRef](#)]
8. Cheng, P.M.; Zhang, G.J.; Zhang, J.Y.; Liu, G.; Sun, J. Coupling effect of intergranular and intragranular particles on ductile fracture of Mo-La₂O₃ alloys. *Mater. Sci. Eng. A* **2015**, *640*, 320–329. [[CrossRef](#)]
9. Wang, L.; Liu, G.; Sun, J. Effects of La₂O₃ and annealing temperature on grain size and mechanical properties of Mo alloys. *Mater. Res. Express* **2017**, *4*, 116515. [[CrossRef](#)]
10. Yang, X.; Tan, H.; Lin, N.; Li, Z.; He, Y. The influences of La doping method on the microstructure and mechanical properties of Mo alloys. *Int. J. Refract. Met. Hard Mater.* **2015**, *51*, 301–308. [[CrossRef](#)]
11. Yang, X.; Tan, H.; Lin, N.; Li, Z.; He, Y. Effects of the lanthanum content on the microstructure and properties of the molybdenum alloy. *Int. J. Refract. Met. Hard Mater.* **2016**, *61*, 179–184. [[CrossRef](#)]
12. Zhang, G.J.; Sun, Y.J.; Zuo, C.; Wei, J.F.; Sun, J. Microstructure and mechanical properties of multi-components rare earth oxide-doped molybdenum alloys. *Mater. Sci. Eng. A* **2008**, *483*, 350–352. [[CrossRef](#)]
13. Cockeram, B.V. The fracture toughness and toughening mechanism of commercially available unalloyed molybdenum and oxide dispersion strengthened molybdenum with an equiaxed, large grain structure. *Metall. Mater. Trans. A* **2009**, *40*, 2843–2860. [[CrossRef](#)]
14. Chen, C.; Wang, S.; Jia, Y.L.; Wang, M.P.; Li, Z.; Wang, Z.X. The microstructure and texture of Mo-La₂O₃ alloys with high transverse ductility. *J. Alloy Compd.* **2014**, *589*, 531–538. [[CrossRef](#)]
15. Endo, M.; Kimura, K.; Udagawa, T.; Tanabe, S.; Seto, H. The effects of doping molybdenum wire with rare-earth elements. *High Temp. High Press.* **1990**, *21*, 129–137.
16. Zhang, J.; Liu, L.; Zhou, M.; Hu, Y.; Zuo, T. Fracture toughness of sintered Mo-La₂O₃ alloy and the toughening mechanism. *Int. J. Refract. Met. Hard Mater.* **1999**, *17*, 405–409.
17. Chen, P.; Qin, M.; Zhang, D.; Chen, Z.; Jia, B.; Wan, Q.; Wu, H.; Qu, X. Combustion synthesis and excellent photocatalytic degradation properties of W₁₈O₄₉. *CrystEngComm* **2015**, *17*, 5889–5894. [[CrossRef](#)]
18. Huang, M.; Qin, M.; Chen, P.; Jia, B.; Chen, Z.; Li, R.; Liu, Z.; Qu, X. Facile preparation of network-like porous hematite (α -Fe₂O₃) nanosheets via a novel combustion-based route. *Ceram. Int.* **2016**, *42*, 10380–10388. [[CrossRef](#)]
19. Bakrania, S.D.; Miller, T.A.; Perez, C.; Wooldridge, M.S. Combustion of multiphase reactants for the synthesis of nanocomposite materials. *Combust. Flame* **2007**, *148*, 76–87. [[CrossRef](#)]

20. Wu, H.; Qin, M.; Chu, A.; Cao, Z.; Chen, P.; Liu, Y.; Qu, X. Effect of urea on the synthesis of Al-doped ZnO nanoparticle and its adsorptive properties for organic pollutants. *Mater. Res. Bull.* **2016**, *75*, 78–82. [[CrossRef](#)]
21. Cao, Z.; Qin, M.; Gu, Y.; Jia, B.; Chen, P.; Qu, X. Synthesis and characterization of Sn-doped hematite as visible light photocatalyst. *Mater. Res. Bull.* **2016**, *77*, 41–47. [[CrossRef](#)]
22. Chen, P.; Qin, M.; Liu, Y.; Jia, B.; Cao, Z.; Wan, Q.; Qu, X. Superior optical properties of Fe³⁺-W₁₈O₄₉ nanoparticles prepared by solution combustion synthesis. *New J. Chem.* **2015**, *39*, 1196–1201. [[CrossRef](#)]
23. Gu, S.; Qin, M.; Zhang, H.; Ma, J.; Wu, H.; Qu, X. Facile solution combustion synthesis of MoO₂ nanoparticles as efficient photocatalysts. *CrystEngComm* **2017**, *19*, 6516–6526. [[CrossRef](#)]
24. Gangwar, B.P.; Palakollu, V.; Singh, A.; Kanvah, S.; Sharma, S. Combustion synthesized La₂O₃ and La(OH)₃: recyclable catalytic activity towards Knoevenagel and Hantzsch reactions. *RSC Adv.* **2014**, *4*, 55407–55416. [[CrossRef](#)]
25. Singh, A.; Palakollu, V.; Pandey, A.; Kanvah, S.; Sharma, S. Green synthesis of 1,4-benzodiazepines over La₂O₃ and La(OH)₃ catalysts: possibility of Langmuir–Hinshelwood adsorption. *RSC Adv.* **2016**, *6*, 103455–103462. [[CrossRef](#)]
26. Nowicki, W.; Piskuła, Z.S.; Kuźma, P.; Kirszensztejn, P. Synthesis and characterization of a binary system La₂O₃–SiO₂ prepared by combustion method. *J. Sol Gel Sci. Technol.* **2017**, *82*, 574–580. [[CrossRef](#)]
27. Gu, S.; Qin, M.; Zhang, H.; Ma, J.; Qu, X. Preparation of Mo nanopowders through hydrogen reduction of a combustion synthesized foam-like MoO₂ precursor. *Int. J. Refract. Met. Hard Mater.* **2018**, *76*, 90–98. [[CrossRef](#)]
28. Wang, L.; Zhang, G.H.; Wang, J.S.; Chou, K.C. Study on hydrogen reduction of ultrafine MoO₂ to produce ultrafine Mo. *J. Phys. Chem. C* **2016**, *120*, 4097–4103. [[CrossRef](#)]
29. Ressler, T.; Jentoft, R.E.; Wienold, J.; Günter, M.M.; Timpe, O. In situ XAS and XRD studies on the formation of Mo suboxides during reduction of MoO₃. *J. Phys. Chem. B* **2000**, *104*, 6360–6370. [[CrossRef](#)]
30. Liang, C.; Ying, P.; Li, C. Nanostructured β-Mo₂C prepared by carbothermal hydrogen reduction on ultrahigh surface area carbon material. *Chem. Mater.* **2002**, *14*, 3148–3151. [[CrossRef](#)]
31. Yang, Y.; Luo, M.; Xing, Y.; Wang, S.; Zhang, W.; Lv, F.; Li, Y.; Zhang, Y.; Wang, W.; Guo, S. A Universal strategy for intimately coupled carbon nanosheets/MoM nanocrystals (M = P, S, C, and O) hierarchical hollow nanospheres for hydrogen evolution catalysis and sodium-ion storage. *Adv. Mater.* **2018**, *30*, 1706085. [[CrossRef](#)] [[PubMed](#)]



© 2018 by the authors. Licensee MDPI, Basel, Switzerland. This article is an open access article distributed under the terms and conditions of the Creative Commons Attribution (CC BY) license (<http://creativecommons.org/licenses/by/4.0/>).